ADVANCED ENERGY MATERIALS
www.advenergymat.de

Conductive Metal–Organic Frameworks Selectively Grown on Laser-Scribed Graphene for Electrochemical Microsupercapacitors

Hao Wu, Wenli Zhang, Sharath Kanadambeth, Osama Shekhah, Mohamed Eddaoudi,* and Husam N. Alshareef*

Conductive 2D metal–organic frameworks (MOFs) have merits beyond traditional MOFs for electrochemical applications, but reports on using MOFs as electrodes for electrochemical microsupercapacitors (MSCs) are practically non-existent. In this work, a Ni-catecholate-based MOF (Ni-CAT MOF) having good conductivity and exhibiting redox chemistry in the positive and negative voltage windows is developed. A novel process is developed to selectively grow the conductive Ni-CAT MOF on 3D laser scribed graphene (LSG). The LSG with its superior wettability serves as a functional matrix-current collector for the hybridization of conductive Ni-CAT MOF nanocrystals. Impressively, MSCs fabricated using the hybrid LSG/Ni-CAT MOF show significant improvement compared with MOF-free LSG electrodes. Specifically, the LSG/Ni-CAT MOF electrodes can deliver MSCs with a wide operating voltage (1.4 V), high areal capacitance (15.2 mF cm^{-2}), energy density (4.1 µWh cm^{-2}), power density (7 mW cm^{-2}), good rate performance, and decent cycling stability. This work opens up an avenue for developing electrochemical microsupercapacitors using conductive MOFs electrodes.

1. Introduction

Miniaturized rechargeable energy storage systems are in high demand to keep up with the rapid development in portable electronics, implantable microdevices, sensor networks, internet of things, etc.[1–3] Electrochemical microsupercapacitors (MSCs) are one promising solution for on-chip micropower units in self-powered devices.[4–7] Recently, laser scribed graphene (LSG) has been demonstrated as a promising electrode for electrochemical MSCs.[8,9] It provides an efficient direct-write process to generate the desired patterns, thus avoiding complicated photolithography techniques and time-consuming multi-stage processes.[10–16] Previous studies have taken advantage of this approach for direct acquisition of electroactive materials such as reduced graphene oxide and 3D porous multilayer graphene through one-step carbonization of polymers (e.g., polyimide film).[17–19] Nevertheless, the capacitance of the bare 3D porous LSG obtained through laser scribing process is limited.[20–22] To address this issue, prudent implementations such as integration of capacitive materials (e.g., MnO_2), heterogeneous atom doping (e.g., N), metal coating (e.g., Au) have been used to improve the electrochemical behavior of LSG. These approaches work by increasing redox activity, specific active sites, and conductivity.[22–28] Inherently, the laser graphitization process used to make LSG endows the 3D graphene with abundant pores and defects along with the transformation of the sp^3-carbon atoms of the polymer to the sp^2-carbon species.[29] Appropriate surface functionalization of graphene has provided immense opportunities for the immobilization of low dimensional nanomaterials.[30–32] Similarly, the rough and defective LSG surfaces are expected to be served as conductive platforms for coupling capacitive moieties.

Metal–organic frameworks (MOFs), a new class of porous material, represent one of the promising electrode materials for electrochemical energy storage application due to their inherent porosity, open pore framework structure, and ultrahigh surface area.[33–40] Particularly, the conductive subgroup of MOFs possesses merits beyond the traditional MOFs because they can lead to faster electron transport during electrochemical reactions.[41,42] The effective π–π stacking between the 2D MOF layers allows for long range of π–π and π–d orbital overlaps, which imparts exceptional charge transport properties. This area has seen a surge of research activity after the exciting demonstration of supercapacitors whose electrodes are made solely from conductive 2D MOFs.[41,42] Yet, no studies on electrochemical microsupercapacitors using conductive MOF

Dr. H. Wu, Dr. W. Zhang, Prof. H. N. Alshareef
Materials Science and Engineering
Physical Science and Engineering Division
King Abdullah University of Science and Technology (KAUST)
Thuwal 23955-6900, Saudi Arabia
E-mail: husam.alshareef@kaust.edu.sa
Dr. S. Kanadambeth, Dr. O. Shekhah, Prof. M. Eddaoudi
Advanced Membranes and Porous Materials Center
Physical Science and Engineering
Functional Materials Design, Discovery and Development (FMD^3)
King Abdullah University of Science and Technology (KAUST)
Thuwal 23955-6900, Saudi Arabia
E-mail: mohamed.eddaoudi@kaust.edu.sa
The ORCID identification number(s) for the author(s) of this article can be found under https://doi.org/10.1002/aenm.201900482.

DOI: 10.1002/aenm.201900482

electrodes have been established so far, which might be attributed to the following concerns. First, nearly all the conductive MOFs reported have been prepared in microcrystalline form, which is commonly patterned by photolithography and inkjet/screen printing.[1–3] These technologies require thermal evaporation/sputtering and etching processes, during which MOFs internal structure may degrade. Secondly, selective growth of conductive 2D MOFs on the desired substrates remains a great challenge, though constructing suitably modified surfaces might be an alternative strategy for the selective growth of MOFs on substrates.[34–36,41–43] Furthermore, most of the conductive 2D MOFs have failed to exhibit capacitive properties as positive and negative electrodes simultaneously.[41,42] In the rare cases, where this has been possible, a specific electrolyte and harsh manipulation conditions (e.g., O_2-free environment) were required and/or a narrow potential window was exhibited,[41–43] rendering them as suboptimal electrode materials. The unitary capability of MOFs as either positive or negative electrode material makes it difficult to construct asymmetric devices, where elaborate device fabrication steps are needed. Thus, selective growth of conductive MOFs that can work in both positive and negative voltages can greatly simplify the fabrication of MSCs and increase the energy density.

Herein, we have combined a laser scribing technique with subsequent a low-temperature selective solvothermal growth to fabricate symmetric MSCs with significantly improved electrochemical behavior. The polyimide (PI) film is used as the substrate and carbon source for directly patterning 3D LSG, which is then served as a 3D conductive matrix for the selective growth of 1D conductive Ni-catecholate (Ni-CAT) MOF nanorods. Impressively, the as-prepared LSG/Ni-CAT MOF hybrids work as both positive and negative electrodes, making it possible to fabricate symmetric solid-state MSCs with much-improved capacitance and energy density compared with bare LSG electrodes. Concurrently, the LSG/Ni-MOF hybrid-based MSCs exhibit a good rate performance and cycling stability. This work inspires the development of conductive MOFs as active materials for miniaturized on-chip MSCs with highly enhanced performance.

2. Results and Discussion

The fabrication process of the hybrid LSG/Ni-CAT MOF electrodes and MSCs is schematically illustrated in **Figure 1**a–c. First, a well-established laser scribing technique is adopted for the graphitization of commercial PI film into LSG, which simultaneously served as the support substrate and carbon source to make on-chip LSG patterns. After the exposure to a CO_2 laser (power 4%, see details in the Experimental Section), a dark gray in-plane interdigital pattern is obtained. Raman spectra (Figure S1, Supporting Information) show a low I_D/I_G ratio (≈0.51) and a 2D band which originates from the second order zone-boundary phonons,[22] indicating that few-layer stacked graphene with a high degree of graphitization has been produced. Scanning electron microscopy (SEM) images show the LSG films to have an interlaced porous morphology with the thin graphene sheets approximately perpendicular to the PI substrate (**Figure 2**a; Figure S2, Supporting Information). Numerous nanosized pores are observed in the transmission electron microscopy (TEM) image (Figure S3, Supporting Information), which originate from the gaseous species (e.g., H_2O, CO_2) that evolve during the decomposition of PI and transformation of sp^3-carbon atoms to the sp^2-carbon matrixes.[22] The 3D and porous surfaces of the LSG are ideal for attaching pseudocapacitive moieties such as MOF. Moreover, the wettability and functionality of the host LSG can play a key role in the subsequent growth of MOF crystals, where a good wettability with low surface energy leads to sufficient penetration of growth solutions, and dangling functional groups (e.g., −OH) which provide extra chemical bonds (or nucleation sites) for anchoring metal complexes. The as-prepared LSG shows a hydrophobic surface judging from the large contact angle (Figure S4, Supporting Information), which is tuned to be hydrophilic by a nonthermal O_2-plasma treatment, so as to facilitate the infiltration of the precursor solution for MOF incubation.

Subsequently, Ni-CAT MOF is selected to be deposited on the surface-modified LSG, in view of the following factors: first, as depicted in Figure 1d,e, Ni-CAT has a well-defined structure with two types of 2D layers: the extended honeycomb structure with hexagonal pores and the discrete units. These 2D layers are stacked alternately (i.e., A-B-A-B-..., as shown in Figure 1f,g) driven by the hydrogen bonding and π-interaction, forming permanent open 1D pore channels (≈1.2 nm in size) which can allow the free permeation of electrolytes. Second, the Ni-CAT MOF has a decent electrical conductivity (10^{-1} S cm^{-1}) compared to typical MOFs due to the highly π-conjugated tricatecholate ligands.[44] Though the analogs containing ortho-substituted heteroatoms (−NH_2 or SH) show higher conductivity than that of −OH, the latter is more chemically stable (in different solvents including water and in air below 200 °C) and it is easier to manipulate its structure.[41–44] Third, Ni-based crystals are smaller in size compared to those of Co and Cu-based ones,[44] which could be advantageous for forming more uniform dispersion/coating on the LSG surface. In light of these potential advantages, we have focused on the LSG/Ni-CAT MOF hybrid to demonstrate the MOF feasibility in MSCs. Considering that the dimethylformamide (DMF) is a polar aprotic solvent that facilitates the deprotonation reaction,[45–47] a modified solvothermal strategy with extra DMF in the solvent was developed for MOF deposition. The black-gray pattern turns into dark blue after the growth (inset of Figure 2b), and tiny uniform nanorods are anchored tightly on the LSG sheets, as shown in the SEM and TEM images (Figure 2b,c; Figure S5, Supporting Information). The length and diameter of the nanorods are around 1 μm and tens of nanometers, respectively. The high-resolution TEM images in Figure 2d,e display clearly the ordered channels and pores (≈1.2 nm) of the typical nanorods along with the incident electron beam perpendicular or parallel to the channels, where some defects are observed in the nanorods (Figure S6, Supporting Information). These features are in agreement with that of the Ni-CAT MOF nanorods reported previously.[44] Notably, the conductivity is measured to be ≈0.01 S cm^{-1} using compressed pellets of small MOF crystals (see details in the Experimental Section), which is nearly eight orders of magnitude more conductive than typical MOFs.[44,48] Moreover, the X-ray diffraction (XRD) patterns are recorded for both bare LSG and nanorod powders collected after 4 and 8 h reaction time,

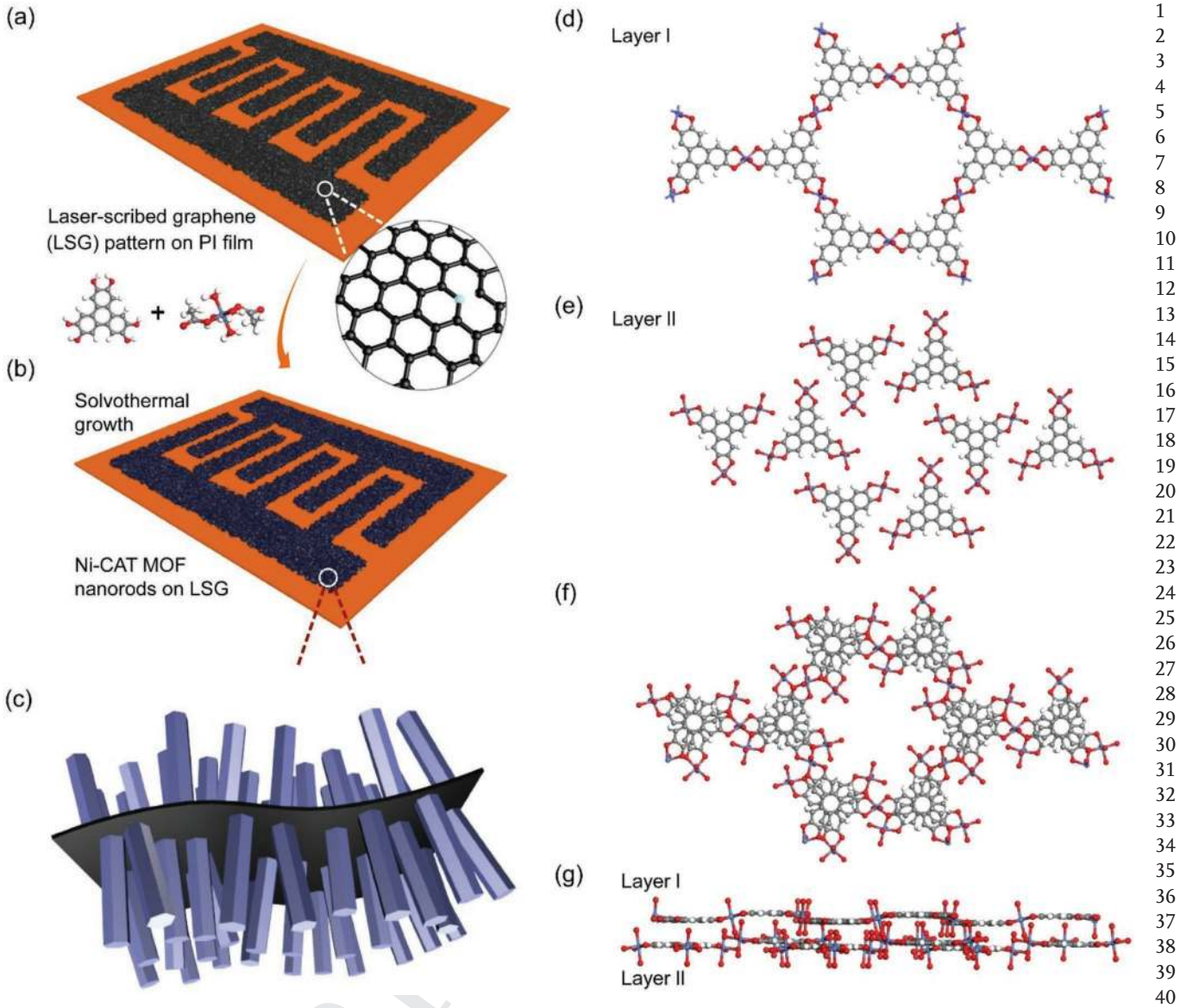

Figure 1. Schematic and structural illustration of LSG/Ni-CAT MOF hybrid. a) In-plane interdigital LSG pattern. b) Solvothermal growth of Ni-CAT MOF nanorods. c) Structure of LSG/Ni-CAT MOF. d,e) View of the two layers of Ni-CAT MOF structure along the *c*-axis. f,g) View of the Ni-CAT MOF stacked layers along *c*-axis and [110] direction, respectively. Color code: C, gray; O, red; H, white; Ni, blue.

as shown in Figure 2f. The LSG shows a main peak located at ≈26°, corresponding to the typical (002) reflection of the graphene. The XRD patterns of the nanorods are well-matched with that of the Ni-CAT MOFs.[44] Meanwhile, all the absorption bands observed in the Fourier transform infrared (FTIR) spectroscopy can be assigned to the vibration features of the bonds in Ni-CAT MOFs (Figure 2g), further providing strong evidence of the formation of Ni-CAT MOFs on the LSG (denoted as LSG/Ni-CAT hereafter). Notably, prolonged incubation time (8 h) results in decreased crystallinity according to the XRD results, which might degrade the electrochemical behaviors.

The mass loading of the Ni-CAT MOF nanorods after different growth time was recorded (**Figure 3**a), to determine the optimal loading density for the electrochemical performance. It can be seen from Figure 3a that the mass loading increases dramatically within the first 2 h, but slows down hereafter. The N_2-sorption isothermal diagrams of the microcrystalline powders collected after 4 and 8 h are of a mixed I/IV type,[22] indicating the existence of mesopores along with the typical micropores of the MOFs (Figure 3b). The mesoporous portion is increased with longer growth time (from 4 to 8 h), upon which the corresponding Brunauer–Emmett–Teller (BET) surface area is decreased from 212 to 194 $m^2\ g^{-1}$ (based on the micropore range). Notably, many grain particles and nanorods with varied lengths and diameters are observed in the powder samples (Figure S7, Supporting Information), while tidier and uniform rods of Ni-CAT are observed for growth on LSG, which probably possess fewer defects and thus larger surface areas. X-ray photoelectron spectroscopy (XPS) spectra were then collected to verify the valence state of the elements. In the

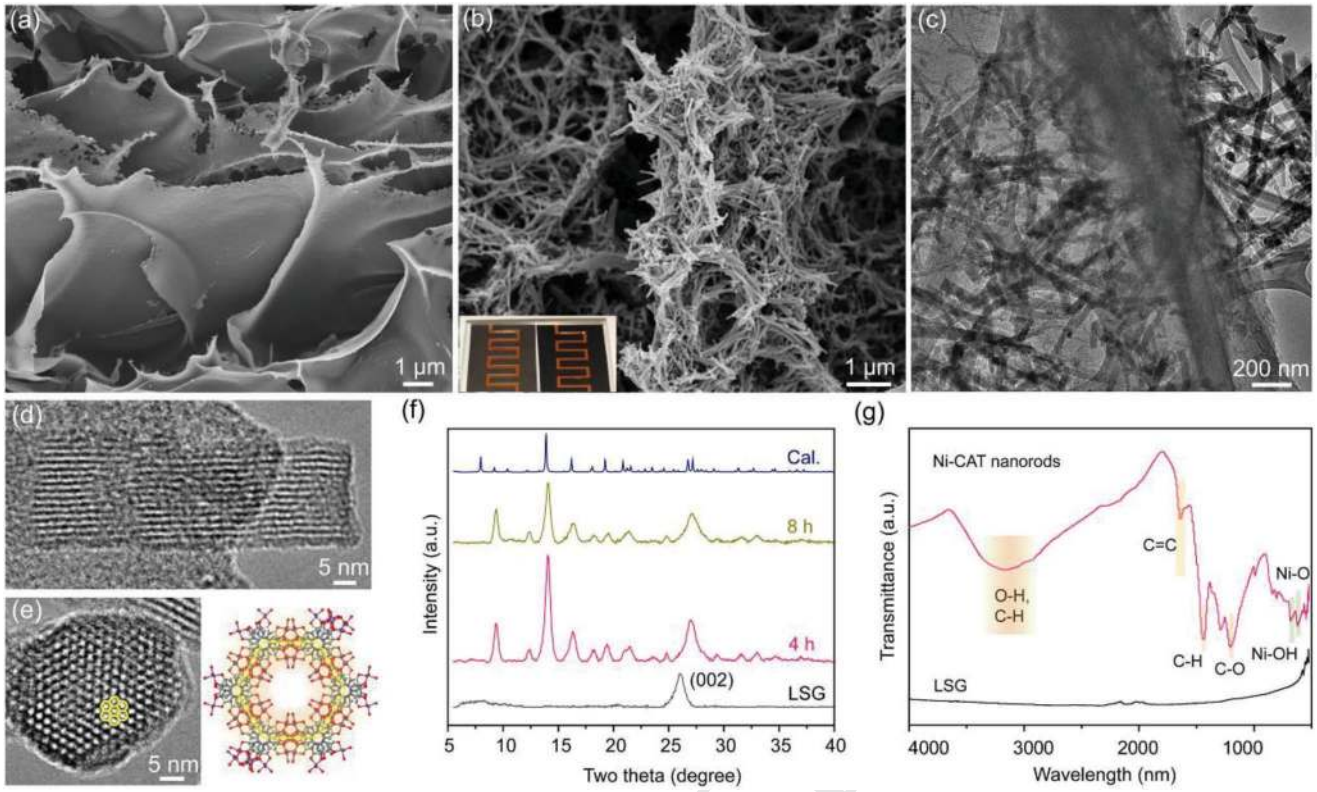

Figure 2. Morphology and composition characterization. a,b) SEM images of LSG and LSG/Ni-CAT MOF, respectively. c) TEM image of LSG/Ni-CAT MOF. d,e) Typical high resolution TEM images of Ni-CAT nanorod with incident electron beam perpendicular and parallel to the channels, respectively. f) XRD patterns of LSG and Ni-CAT MOF nanorods (baseline corrected). g) FTIR spectra of LSG and Ni-CAT MOF.

C 1s spectrum of the LSG, the main deconvoluted peak (76%) is located at 284.4 eV, corresponding to the C=C bonds, while a small portion at 286 eV (≈21%) can be assigned to C—O bonds (Figure 3c).[22] The O 1s spectrum confirms the existence of C—O bonds (Figure 3e), implying that the LSGs are dominated by the sp^2 carbon, with some O dopants and oxygenated groups that can be attributed to the air ambient graphitization and plasma post-treatment. After the Ni-CAT nanorods coating, the C—O peak at 285.9 eV becomes dominant in the C 1s spectrum thanks to the plentiful catecholates, while the increase of the C=O (287.3 eV) and O—C=O (289.2 eV) proportion might be attributed to the termination of the coordination-unsaturated catecholates (Figure 3d).[22,49] The intensity of O 1s peak is greatly increased, as a result of the contribution of lattice O (O—Ni) and C—O of the coordinated catecholates (Figure 3f).[50] The altered features in the XPS spectra are in agreement with the emergence of Ni-CAT MOF species.

Electrochemical tests in a three-electrode mode were first conducted to investigate the capacitive performance of both bare LSG and LSG/Ni-CAT MOF electrodes. As shown in the cyclic voltammetry (CV) curves, the LSG/Ni-CAT electrode exhibits capacitive capabilities as both negative and positive electrode in a neutral aqueous LiCl electrolyte with a Ag/AgCl reference electrode (**Figure 4**a). Thus, it shows great potential as electrode for symmetric capacitors. The CV curves tested in a two-electrode configuration in aqueous electrolyte display analogical quasirectangular shapes (Figure 4b), implying an electrical double-layer capacitive storage mechanism and a wide working potential window (up to 1.4 V). As a comparison, the bare LSG electrode shows a much smaller current density than that of the LSG/Ni-CAT composite (Figure 4c), indicating the substantial capacitance contribution from the Ni-CAT MOFs. The galvanostatic charge/discharge (CD) curves were measured to evaluate the areal capacitances of both LSG and LSG/Ni-CAT electrodes (Figure 4d). It is obvious that the LSG/Ni-CAT shows a better capacitive behavior with a specific areal capacitance of ≈8.5 mF cm^{-2} based on the integrated discharge area, which is over three times higher than that of the bare LSG (2.7 mF cm^{-2}). It should, therefore, be possible to fabricate high-performance solid-state symmetric MSCs by virtue of the predominant capacitive behavior of the hybrid LSG/Ni-CAT electrodes.

A solid-state LiCl/PVA electrolyte was prepared for the fabrication of MSCs with interdigital electrode structure (see details in the Experimental Section). The CV curves of the LSG/Ni-CAT device indicate that the capacitance increases with reaction time, while an optimal value is reached at 4 h (**Figure 5**a). Prolonged reaction time up to 8 h results in degradation of the capacitive performance (Figure S8, Supporting Information), in agreement with the decreased crystallinity and surface area. Thus, the devices with a deposition time of 4 h were selected for the following electrochemical tests. The device exhibits good quasirectangular CV curves at different scan rates (Figure 5b), with the area becoming larger when the scan rate is increased, demonstrating the good electrical double-layer capacitive storage performance. By contrast, the CD curves of the LSG/Ni-CAT based device show a sharp improvement compared

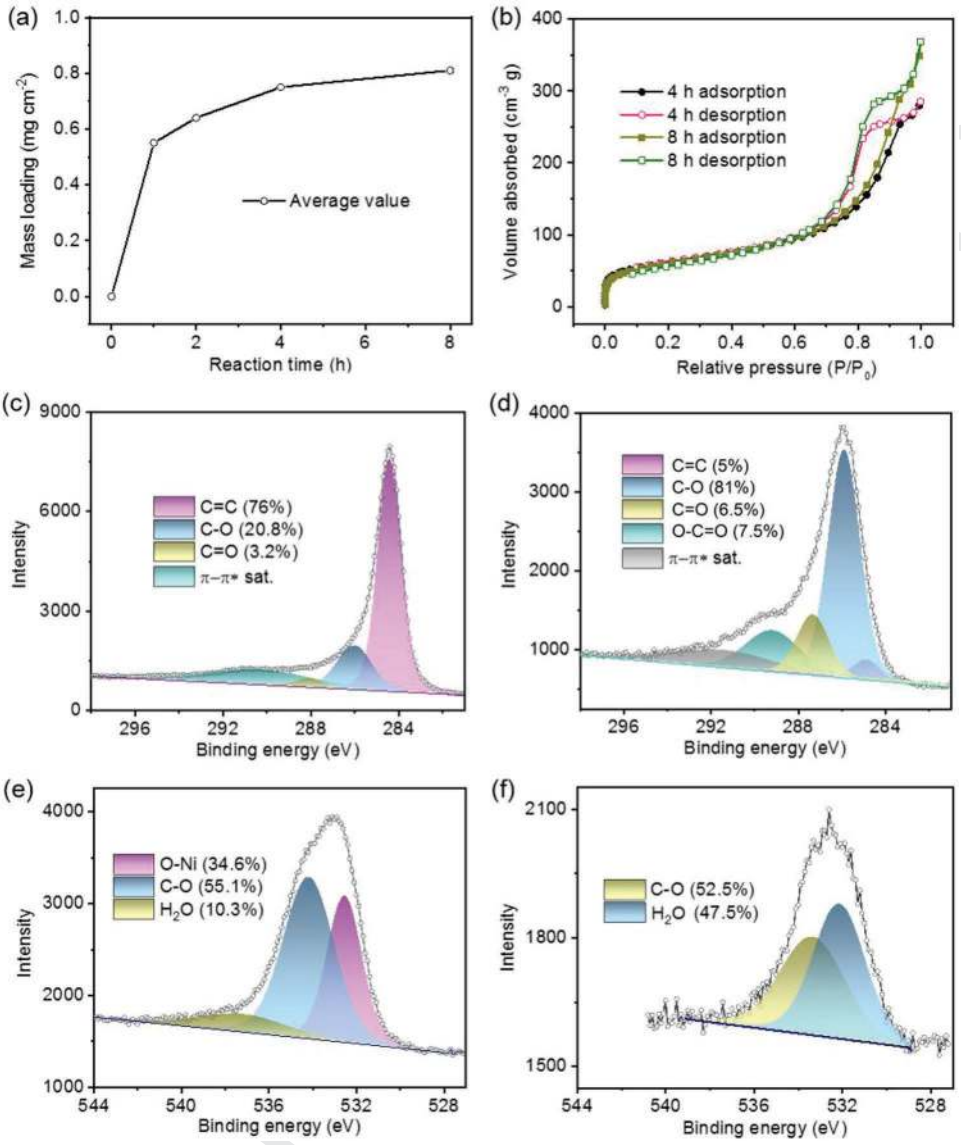

Figure 3. Surface characterization and analysis. a) Mass loading of Ni-CAT MOF. b) N_2 isothermal curves Ni-CAT MOF. c,e) XPS C 1s spectra of LSG and LSG/Ni-CAT MOF, respectively. d,f) XPS O 1s spectra of LSG and LSG/Ni-CAT MOF, respectively.

to that of the bare LSG (Figure 5c). To investigate the charge transfer dynamics, the electrochemical impedance spectroscopy analysis was performed on both types of devices (Figure S9, Supporting Information). As shown in the Nyquist plots, the LSG/Ni-MOF hybrid-based MSC shows a smaller equivalent series resistance (R_s, 11.8 Ω) and semicircle (charge transfer resistance, R_{ct}, 0.6 Ω), as well as a shorter diffusion region compared to that of bare LSG (R_s, 15.8 Ω; R_{ct}, 0.8 Ω), indicating a faster charge transfer and more efficient electrolyte ion diffusion.[9,51] Moreover, the device based on the LSG/Ni-CAT electrodes exhibits a slow self-discharging rate (decreased by 20% after 10 h, Figure S10, Supporting Information), which is competitive with literature.[52] The rate performance of the LSG/Ni-CAT device is evaluated at various charge/discharge current densities (Figure 5d), which overwhelmingly outperforms the bare LSG (Figure S11, Supporting Information). The comparison of the areal capacitance of the two devices is summarized as Figure 5e. It can be clearly seen that MSCs using LSG/Ni-CAT electrodes have nearly one order of magnitude higher areal capacitance compared to bare LSG electrodes at all current densities (e.g., 15.2 vs 0.76 mF cm^{-2} at 0.2 mA cm^{-2}; 10.2 vs 0.71 mF cm^{-2} at 1 mA cm^{-2}. Due to the high specific areal capacitance and wide operating voltage window, a high areal energy density ($E_{A,\,max} \approx 4.1$ μWh cm^{-2}) and power density ($P_{A,\,max} \approx 7$ mW cm^{-2}) are reached in the LSG/Ni-CAT MSCs, which is competitive with MSCs using various types of composite electrodes (Figure S12, Supporting Information).[4,22,24,53] Moreover, the cycling stability of the device was evaluated by the galvanostatic CD at 2 mA cm^{-2}, as shown in Figure 5f and Figure S13 (Supporting Information). The capacitance retained after 5000 cycles for the MOF-based electrodes is around 81% and 87% in the aqueous and gel electrolytes, respectively.[34–36,41–43] SEM and TEM images after cycling

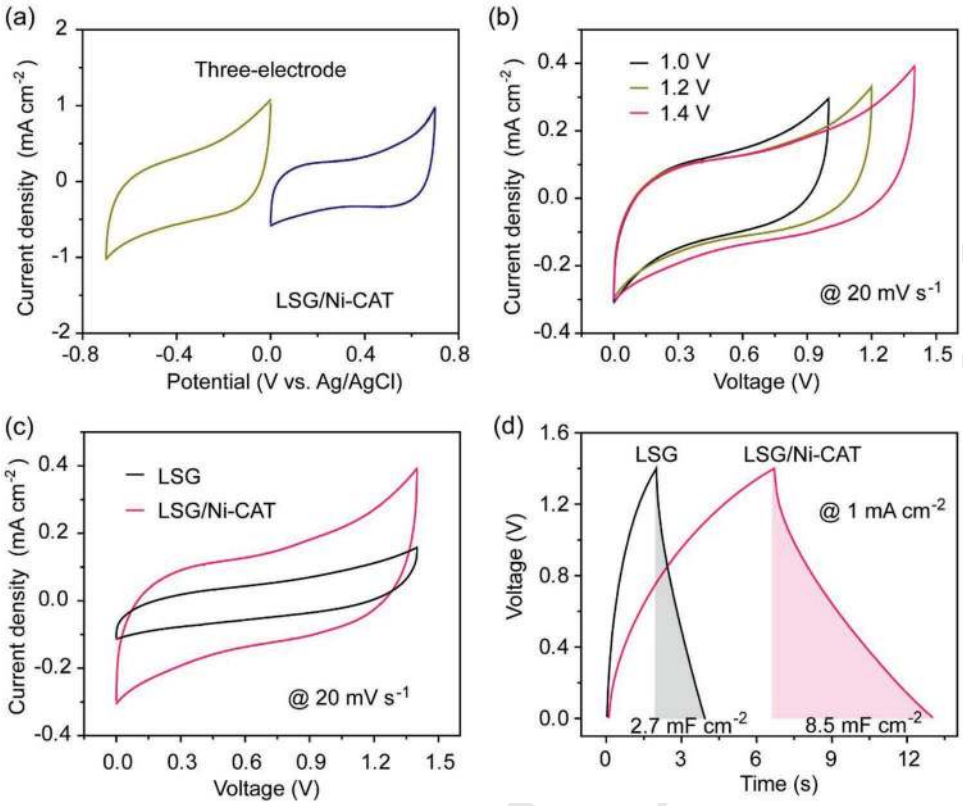

Figure 4. Electrochemical tests in aqueous electrolyte. a) CV curves of LSG/Ni-CAT MOF electrode in a 3 M LiCl electrolyte in three-electrode mode. b) CV curves of LSG/Ni-CAT MOF in two-electrode mode. c) CV comparison of bare LSG and LSG/Ni-CAT MOF. d) Galvanostatic CD curves of bare LSG and LSG/Ni-CAT MOF.

reveal that the morphology of Ni-CAT MOF is retained, while the crystallinity has slightly decreased (Figures S14 and S15, Supporting Information). The drop in capacitance is likely due to the oxidation of the Ni centers (increased lattice O—Ni bonds, Figure S16, Supporting Information), leading to the deterioration of the Ni-CAT MOF electrode (Figure S17, Supporting Information).

3. Conclusion

We have demonstrated microsupercapacitors using MOF electrodes for the first time. The Ni-CAT MOF exhibits good conductivity, redox activity in the negative and positive voltage windows, resulting in large voltage window operation. The Ni-CAT MOF was selectively grown on patterned 3D LSG electrodes through a combined laser-scribing and a selective solvothermal deposition process. The LSG serves as the conductive 3D matrix for the selective and uniform deposition of conductive Ni-CAT MOF nanorods by enriching the surface wettability through plasma treatment. The as-synthesized microsupercapacitors using LSG/Ni-CAT MOF electrodes exhibit superior capacitance, power density, and rate performance compared with bare LSG electrodes, while retaining good cycling stability. This work shows that conductive MOF electrodes can serve as electrodes for high-performance electrochemical microsupercapacitors for miniaturized energy storage systems.

4. Experimental Section

Fabrication of LSG Pattern: The LSG patterns were prepared by a CO_2 laser cutting technique (Universal X-660 laser cutting platform), with a beam size of ≈100 µm and laser power of 4%. The scan rate and the focused laser beam distance were set as 3% and 3 mm, respectively. PI film was used directly as the substrate and as the carbon source. The thickness of the PI film is ≈200 µm.

Synthesis of Ni-CAT Nanorods (NRs) on LSG: Prior to the Ni-CAT MOF NRs growth, the LSG on PI film was treated with O_2-plasma under 700 mTorr pressure (power 45 W) for 1.5 min. The Ni-CAT nanorods were synthesized with a modified solvothermal method.[44] Specifically, a mixture of nickel(II) acetate tetrahydrate (0.02 mmol) and tricatecholate, i.e., 2,3,6,7,10,11-hexahydroxytriphenylene (0.01 mmol) ligand was dissolved in 0.5 mL deionized (DI) water and 0.5 mL DMF solvent, and added in a glass vial. Then, a piece of treated LSG film was put in the glass vial with the LSG facing down and heated at 80 °C for 1 to 8 h. The color of the LSG changed from black-gray to dark blue after the solvothermal process. The as-obtained film was washed with DI water, DMF, and acetone in succession. The final product named LSG/Ni-CAT was dried under vacuum for 20 h at 50 °C. Powders obtained in the growth were collected for the BET and XRD measurements.

Electrochemical Tests of Bare LSG and LSG/Ni-CAT MOF Electrodes in Aqueous Electrolyte: The LSG/Ni-CAT MOF was used as the working electrode for the electrochemical tests in the three-electrode configuration, with a Ag/AgCl electrode and graphite rod as the reference and counter electrode, respectively. The electrolyte used in the three-electrode mode was 3 M LiCl aqueous solution. In the two-electrode configuration, the LSG/Ni-CAT MOF was used as both the positive electrode and the negative electrode by hanging in the aqueous electrolyte. Bare LSG was tested in the same condition for comparison.

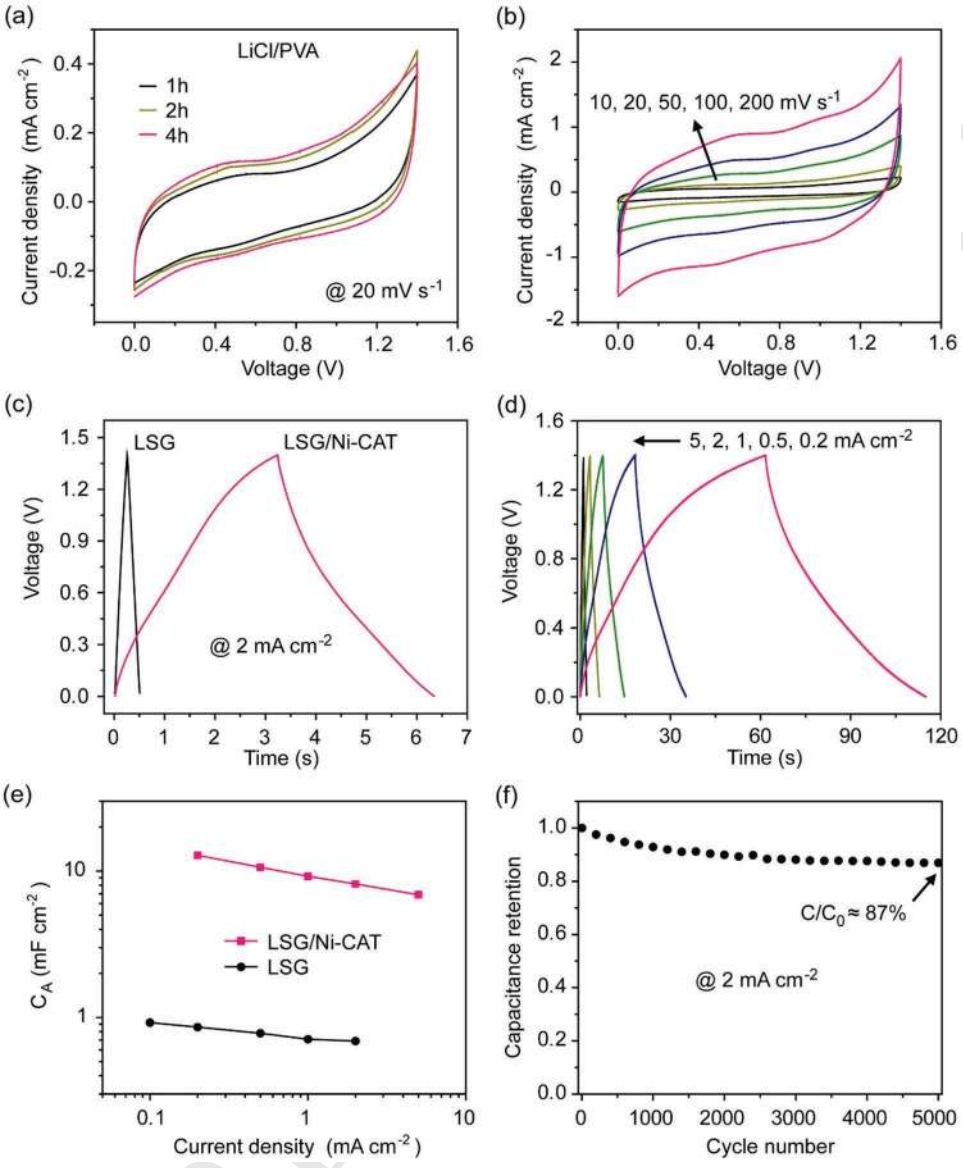

Figure 5. Electrochemical tests of microsupercapacitor devices with gel electrolyte. a) CV curves of LSG/Ni-CAT MOF with different growth periods. b) CV curves of LSG/Ni-CAT MOF at different scanning rates. c) Galvanostatic CD curves of bare LSG and LSG/Ni-CAT MOF. d) Galvanostatic CD curves of LSG/Ni-CAT MOF at different current densities. e) Areal capacitance comparison. f) Cycling stability test of LSG/Ni-CAT MOF device.

Fabrication of Symmetrical Microsupercapacitors: The LiCl/PVA gel electrolyte for the microsupercapacitor devices was prepared by dissolving 1 g PVA powder in 10 mL 3 M LiCl aqueous solution under vigorous stirring at 80 °C until a clear gel is formed. The LSG/Ni-CAT was first immersed in the LiCl/PVA gel electrolyte for 30 min and then taken out for drying in ambient for another 30 min before the measurement. Bare LSG was tested in the same condition for comparison. The electrochemical impedance spectra were recorded at the open-circuit voltage with a voltage amplitude of 10 mV in the frequency range from 100 kHz to 10 mHz. The specific areal capacitances, energy densities, and power densities were calculated via the equations according to the previous reports.[22]

Characterization: SEM images were captured on a field emission scanning electron microscopy (FEI Magellan) operated at 3 kV and 13 pA. TEM images were taken on a transmission electron microscope (FEI, Titan 80–300 ST). XRD patterns were scanned on a Bruker diffractometer with Cu Kα radiation (λ = 1.5406 Å). Raman spectra were collected on a micro-Raman spectrometer (LabRAM ARAMIS, Horiba-Jobin Yvon) using a cobalt laser (473 nm). BET surface area was evaluated by N_2 adsorption–desorption isotherms measured on a N_2 adsorption/desorption analyzer (ASAP 2020, Micrometrics). XPS analysis was performed on a photoelectron spectrometer (Kratos Axis Supra, Shimadzu). FTIR spectra were collected on a Nicolet iS10 FT-IR Spectrometer. Contact angles were captured on a Kruss FM40 EasyDrop contact angle measuring instrument. Conductivity measurement was perfromed based on a compressed pellet of Ni-CAT MOF powder (15 MPa, 200 µm in thickness) using a four-point probe method on a thermoelectric tester RZ2001i (Ozawa Science Co. Ltd., Japan).

Supporting Information

Supporting Information is available from the Wiley Online Library or from the author.

Acknowledgements

H.W. and W.Z. contributed equally to this work. Research reported in this publication was supported by the King Abdullah University of Science and Technology (KAUST).

Conflict of Interest

The authors declare no conflict of interest.

Keywords

conductive, graphene, laser-scribed, metal–organic frameworks, microsupercapacitors

Received: February 9, 2019
Revised: March 15, 2019
Published online:

[1] N. Liu, Y. Gao, *Small* **2017**, *13*, 1701989.
[2] J. Chmiola, C. Largeot, P.-L. Taberna, P. Simon, Y. Gogotsi, *Science* **2010**, *328*, 480.
[3] N. A. Kyerematen, T. Brousse, D. Pech, *Nat. Nanotechnol.* **2017**, *12*, 7.
[4] J. Yoo, S. Byun, C.-W. Lee, C.-Y. Yoo, J. Yu, *Chem. Mater.* **2018**, *30*, 3979.
[5] N. Kurra, B. Ahmed, Y. Gogotsi, H. N. Alshareef, *Adv. Energy Mater.* **2016**, *6*, 1601372.
[6] Y. Da, J. Liu, L. Zhou, X. Zhu, X. Chen, L. Fu, *Adv. Mater.* **2019**, *31*, 1802793.
[7] P. Huang, C. Lethien, S. Pinaud, K. Brousse, R. Laloo, V. Turq, M. Respaud, A. Demortiere, B. Daffos, P. L. Taberna, B. Chaudret, Y. Gogotsi, P. Simon, *Science* **2016**, *351*, 691.
[8] Y. Yue, N. Liu, Y. Ma, S. Wang, W. Liu, C. Luo, H. Zhang, F. Cheng, J. Rao, X. Hu, J. Su, Y. Gao, *ACS Nano* **2018**, *12*, 4224.
[9] Y. Shao, J. Li, Y. Li, H. Wang, Q. Zhang, R. B. Kaner, *Mater. Horiz.* **2017**, *4*, 1145.
[10] M. Zhu, Y. Huang, Y. Huang, H. Li, Z. Wang, Z. Pei, Q. Xue, H. Geng, C. Zhi, *Adv. Mater.* **2017**, *29*, 1605137.
[11] M. Beidaghi, C. Wang, *Adv. Funct. Mater.* **2012**, *22*, 4501.
[12] W. J. Hyun, E. B. Secor, C.-H. Kim, M. C. Hersam, L. F. Francis, C. D. Frisbie, *Adv. Energy Mater.* **2017**, *7*, 1700285.
[13] L. Li, Z. Lou, W. Han, D. Chen, K. Jiang, G. Shen, *Adv. Mater. Technol.* **2017**, *2*, 1600282.
[14] S. M. Mirvakili, I. W. Hunter, *Adv. Mater.* **2017**, *2*, 91700671.
[15] G. Nystrom, A. Marais, E. Karabulut, L. Wagberg, Y. Cui, M. M. Hamedi, *Nat. Commun.* **2015**, *6*, 7259.
[16] Z. Niu, L. Zhang, L. Liu, B. Zhu, H. Dong, X. Chen, *Adv. Mater.* **2013**, *25*, 4035.
[17] M. F. El-Kady, V. Strong, S. Dubin, R. B. Kaner, *Science* **2012**, *335*, 1326.
[18] L. Li, J. Zhang, Z. Peng, Y. Li, C. Gao, Y. Ji, R. Ye, N. D. Kim, Q. Zhong, Y. Yang, H. Fei, G. Ruan, J. M. Tour, *Adv. Mater.* **2016**, *28*, 838.
[19] W. Gao, N. Singh, L. Song, Z. Liu, A. L. Reddy, L. Ci, R. Vajtai, Q. Zhang, B. Wei, P. M. Ajayan, *Nat. Nanotechnol.* **2011**, *6*, 496.
[20] M. F. El-Kady, R. B. Kaner, *Nat. Commun.* **2013**, *4*, 1475.
[21] X. Shi, Z. S. Wu, J. Qin, S. Zheng, S. Wang, F. Zhou, C. Sun, X. Bao, *Adv. Mater.* **2017**, *29*, 1703034.
[22] W. Zhang, Y. Lei, F. Ming, Q. Jiang, P. M. F. J. Costa, H. N. Alshareef, *Adv. Energy Mater.* **2018**, *8*, 1801840.
[23] F. Zhang, E. Alhajji, Y. Lei, N. Kurra, H. N. Alshareef, *Adv. Energy Mater.* **2018**, *8*, 1800353.
[24] K. Shen, J. Ding, S. Yang, *Adv. Energy Mater.* **2018**, *8*, 1800408.
[25] H. Li, Y. Hou, F. Wang, M. R. Lohe, X. Zhuang, L. Niu, X. Feng, *Adv. Energy Mater.* **2017**, *7*, 1601847.
[26] Z. Peng, R. Ye, J. A. Mann, D. Zakhidov, Y. Li, P. R. Smalley, J. Lin, J. M. Tour, *ACS Nano* **2015**, *9*, 5868.
[27] P. Zhang, F. Zhu, F. Wang, J. Wang, R. Dong, X. Zhuang, O. G. Schmidt, X. Feng, *Adv. Mater.* **2017**, *29*, 1604491.
[28] A. Basu, K. Roy, N. Sharma, S. Nandi, R. Vaidhyanathan, S. Rane, C. Rode, S. Ogale, *ACS Appl. Mater. Interfaces* **2016**, *8*, 31841.
[29] A. Lamberti, F. Clerici, M. Fontana, L. Scaltrito, *Adv. Energy Mater.* **2016**, *6*, 1600050.
[30] B. Luo, L. Zhi, *Energy Environ. Sci.* **2015**, *8*, 456.
[31] R. T. Wang, J. W. Lang, P. Zhang, Z. Y. Lin, X. B. Yan, *Adv. Funct. Mater.* **2015**, *25*, 2270.
[32] H. Xia, C. Hong, B. Li, B. Zhao, Z. Lin, M. Zheng, S. V. Savilov, S. M. Aldoshin, *Adv. Funct. Mater.* **2015**, *25*, 627.
[33] Z. Liang, C. Qu, W. Guo, R. Zou, Q. Xu, *Adv. Mater.* **2018**, *30*, 1702891.
[34] N. Ogihara, Y. Ozawa, O. Hiruta, *J. Mater. Chem. A* **2016**, *4*, 3398.
[35] Y. Yan, Y. Luo, J. Ma, B. Li, H. Xue, H. Pang, *Small* **2018**, *14*, 1801815.
[36] G. Zhu, H. Wen, M. Ma, W. Wang, L. Yang, L. Wang, X. Shi, X. Cheng, X. Sun, Y. Yao, *Chem. Commun.* **2018**, *54*, 10499.
[37] R. R. Salunkhe, C. Young, J. Tang, T. Takei, Y. Ide, N. Kobayashi, Y. Yamauchi, *Chem. Commun.* **2016**, *52*, 4764.
[38] W. Zhang, X. F. Jiang, Y. Y. Zhao, A. Carne-Sanchez, V. Malgras, J. Kim, J. H. Kim, S. B. Wang, J. Liu, J. S. Jiang, Y. Yamauchi, M. Hu, *Chem. Sci.* **2017**, *8*, 3538.
[39] C. Young, J. Wang, J. Kim, Y. Sugahara, J. Henzie, Y. Yamauchi, *Chem. Mater.* **2018**, *30*, 3379.
[40] C. Wang, Y. V. Kaneti, Y. Bando, J. Lin, C. Liu, J. Li, Y. Yamauchi, *Mater. Horiz.* **2018**, *5*, 394.
[41] D. Sheberla, J. C. Bachman, J. S. Elias, C. J. Sun, Y. Shao-Horn, M. Dinca, *Nat. Mater.* **2017**, *16*, 220.
[42] D. Feng, T. Lei, M. R. Lukatskaya, J. Park, Z. Huang, M. Lee, L. Shaw, S. Chen, A. A. Yakovenko, A. Kulkarni, J. Xiao, K. Fredrickson, J. B. Tok, X. Zou, Y. Cui, Z. Bao, *Nat. Energy* **2018**, *3*, 30.
[43] W.-H. Li, K. Ding, H.-R. Tian, M.-S. Yao, B. Nath, W.-H. Deng, Y. Wang, G. Xu, *Adv. Funct. Mater.* **2017**, *27*, 1702067.
[44] M. Hmadeh, Z. Lu, Z. Liu, F. Gándara, H. Furukawa, S. Wan, V. Augustyn, R. Chang, L. Liao, F. Zhou, E. Perre, V. Ozolins, K. Suenaga, X. Duan, B. Dunn, Y. Yamamto, O. Terasaki, O. M. Yaghi, *Chem. Mater.* **2012**, *24*, 3511.
[45] O. Shekhah, J. Liu, R. A. Fisher, Ch. Wöll, *Chem. Soc. Rev.* **2011**, *40*, 1081.
[46] J. Liu, O. Shekhah, X. Stammer, H. K. Arslan, B. Liu, B. Schüpbach, A. Terfort, C. Wöll, *Materials* **2012**, *5*, 1581.
[47] V. Chernikova, O. Shekhah, M. Eddaoudi*ACS Appl. Mater. Interfaces* **2016**, *8*, 20459.
[48] L. Sun, M. G. Campbell, M. Dincă, *Angew. Chem., Int. Ed.* **2016**, *55*, 3566.
[49] R. R. Salunkhe, J. Tang, Y. Kamachi, T. Nakato, J. H. Kim, Y. Yamauchi, *ACS Nano* **2015**, *9*, 6288.
[50] H. Wu, X. Lu, G. Zheng, G. W. Ho, *Adv. Energy Mater.* **2018**, *8*, 1702704.
[51] B.-A. Mei, O. Munteshari, J. Lau, B. Dunn, L. Pilon, *J. Phys. Chem. C* **2018**, *122*, 194.
[52] Q. Jiang, C. Wu, Z. Wang, A. C. Wang, J. H. He, Z. L. Wang, H. N. Alshareef, *Nano Energy* **2018**, *45*, 266.
[53] J. Lin, Z. Peng, Y. Liu, F. Ruiz-Zepeda, R. Ye, E. L. Samuel, M. J. Yacaman, B. I. Yakobson, J. M. Tour, *Nat. Commun.* **2014**, *5*, 5714.

